Relating defect chemistry and electronic transport in the double perovskite $Ba_{1-x}Gd_{0.8}La_{0.2+x}Co_2O_{6-\delta}$ (BGLC)

Einar Vøllestad[1], Matthias Schrade[2], Julie Segalini[3], Ragnar Strandbakke[1], Truls Norby[1]

1: Department of Chemistry, University of Oslo, FERMiO, Gaustadalléen 21, NO-0349 Oslo, Norway.

2: Department of Physics, University of Oslo, FERMiO, Gaustadalléen 21, NO-0316 Oslo, Norway.

3: Marion Technologies, Parc Technologique Delta Sud, 55 Rue Pasteur, 09340 Verniolle, France

Abstract

Rare earth double perovskites comprise a class of functional oxides with interesting physiochemical properties both for low- and high-temperature applications. However, little can be found relating electrical properties with equilibrium thermodynamics of non-stoichiometry and defects. In the present work, a comprehensive and generally applicable defect chemical model is developed to form the link between the defect chemistry and electronic structure of partially substituted BGLC ($Ba_{1-x}Gd_{0.8}La_{0.2+x}Co_2O_{6-\delta}$, $0 \leq x \leq 0.5$). The equilibrium oxygen content of 4 different compositions is determined as a function of pO_2 and temperature by thermogravimetric analysis, and combined with defect chemical modelling to obtain defect concentrations and thermodynamic parameters. Oxidation enthalpies determined by TG-DSC become increasingly exothermic (-50 to -120 kJ mol^{-1}) with increased temperature and oxygen non-stoichiometry for all composition, in excellent agreement with the thermodynamic parameters obtained from the defect chemical model. All compositions display high electrical conductivities (500 to 1000 S cm^{-1}) with shallow pO_2-dependencies and small and positive Seebeck coefficients (3 to 15 µV K^{-1}), indicating high degree of degeneracy of the electronic

charge carriers. The complex electrical properties of BGLC at elevated temperatures is rationalized by a two-band conduction model where highly mobile p-type charge carriers are transported within the valence band, whereas less mobile "n-type" charge carriers are located in narrow Co 3*d* band

1. Introduction

Rare earth double perovskites with the general formula $BaLnCo_2O_{6-\delta}$ have shown great promise as candidate materials for electrode and membrane applications at intermediate to high temperatures.[1-4] The flexibility of the double perovskite structure allows for large variations in cation type and contents, oxygen non-stoichiometry (δ), and effective cobalt valence state, giving rise to high mixed ionic and electronic conductivity and fast surface kinetics.[5] Moreover, we have shown in a recent study that the double perovskite $BaGd_{0.8}La_{0.2}Co_2O_{6-\delta}$ (BGLC) is well suited as steam- and oxygen-electrode material in proton ceramic electrochemical cells, due in part to its ability to incorporate protonic charge carriers under humid conditions.[1]

The low temperature physical properties of the $BaLnCo_2O_{6-\delta}$ family are well understood owing to extensive characterization of their giant magnetoresistance, charge and orbital ordering, and spin state transitions below room temperature.[6, 7] The double perovskites display an ordering of the A-site cations with alternating Ba and Ln layers along the c-axis, which leads to preferential formation of oxygen vacancies in the Ln layer.[7-9] Consequently, cobalt is present in both octahedral and square pyramidal coordination, which is proposed as the origin of many of the interesting electromagnetic properties of these materials.[7] Co^{3+} in 6-coordinated octahedra undergoes a low-spin (LS, t_{2g}^6) to high-spin (HS, $t_{2g}^4e_g^2$) transition at the metal to insulator transition temperature (T_{MI}), while pyramidal Co^{3+} remains in an IS ($t_{2g}^5e_g^1$) state across T_{MI}.[6, 10, 11] The new spin states above T_{MI} increase the electronic degeneracy, and form band states within the band gap of partially filled anti-bonding σ*-bands wherein electronic conduction can occur.[6, 11]

The mechanism for electronic transport at higher temperature is, however, less clear. Positive pO_2 dependencies for the conductivity indicate a predominantly p-type charge transport, attributed to localized small polarons in the form of Co^{4+} states. However, the temperature dependency, and small values of the Seebeck coefficient are more reflective of metallic conduction, which would indicate that the p-type charge carriers are itinerant in nature and that the involved electronic bands have partial filling. Furthermore, the conductivity does not scale linearly with the concentration of Co^{4+} species when changing the oxygen stoichiometry,[12] which must reflect either the presence a parallel conduction path of another electronic charge carrier (in a different band) or that the mobility changes with δ.[13] Taskin *et al*. suggested parallel conduction of both electrons and holes for stoichiometric $BaGdCo_2O_{5.5}$, where the electron holes were considered itinerant and present in a broad valence band, whereas the electrons were considered to occupy a more narrow band of cobalt 3*d* states with a consequent lower mobility than the electron holes.[11]

To elucidate the high temperature behavior of these double perovskites and link the structural and physicochemical properties over a large temperature range, it is useful to develop a defect chemical model. Several approaches have been undertaken to describe the defect chemistry of $BaLnCo_2O_{6-\delta}$ double perovskites, using a simple $LnCoO_3$ perovskite as the reference structure with the introduction of 50% Ba on lanthanide site as an acceptor dopant.[12-18] The ordered oxygen vacancies are then further described by an association reaction between the lanthanide cation and the vacancy. This approach has been shown to accurately predict the oxygen non-stoichiometry in $PrBaCo_2O_{6-\delta}$ (PBCO) and $GdBaCo_2O_{6-\delta}$ (GBCO) at high temperatures.[15-18] However, the model assumes a fully disordered A-site sublattice and does not account for the two distinctly different A-site positions of the structure, and thus incorrectly accounts for the configurational entropy of the cation lattices.

For many applications it may also prove beneficial to alter the A-site cation stoichiometry by aliovalent doping to tune properties such as oxygen stoichiometry, oxide basicity and degree of oxygen disorder. For instance, partial substitution of Ba^{2+} with La^{3+} in BGLC ($Ba_{1-x}Gd_{0.8}La_{0.2+x}Co_2O_{6-\delta}$) can potentially increase the stability of the double perovskite towards acidic gases such as steam and CO_2. Therein, the local oxygen ordering cannot be described as a simple association reaction with the lanthanide cation when the concentration of Ln exceeds

unity, underpinning the need for a more generally applicable defect chemical model for double perovskites.

In this work, we develop a comprehensive defect chemical model, incorporating both variations in A-site cation- and oxygen stoichiometry. The model will be able to explain the effect of pO_2 and temperature on cobalt valence state distribution and total conductivity, here shown to arise from both electrons and electron holes with different mobilities. As our model material, we study the effect of partial substitution of Ba^{2+} with La^{3+} on oxygen non-stoichiometry and electrical properties of $Ba_{1-x}Gd_{0.8}La_{0.2+x}Co_2O_{6-\delta}$ ($0 \leq x \leq 0.5$) and extract thermodynamic parameters from defect chemical modelling and calorimetry.

2. Defect chemistry of $BaLnCo_2O_{6-\delta}$ double perovskites

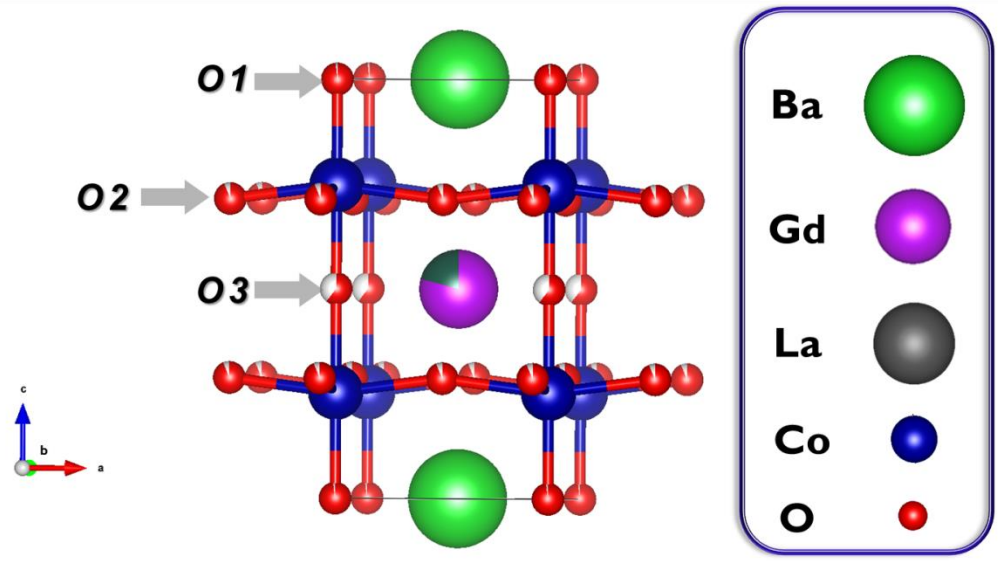

Figure 1: Illustration of the layered double perovskite structure of un-substituted BGLC (x = 0).

To treat the defect chemistry of $Ba_{1-x}Ln_xCo_2O_{6-\delta}$ double perovskites, a proper reference state must first be defined which accounts for the layered double perovskite structure, as depicted in Figure 1. We therefore define our reference state as fully oxidized $BaLnCo_2O_6$, with two

different A-sites (A^{I} and A^{II}) occupied by Ba and Ln, respectively. Ln substituted into the Ba-layer will thus act as a donor ($Ln_{Ba}^{\bullet}$). The reference cobalt valence state in this configuration is defined as $Co^{3.5+}$, reflecting a delocalized electron hole shared between the two cobalt atoms in each unit cell, located in the broad band constituted by the Co_{3d}-O_{2p}-Co_{3d} orbitals.[19, 20] Thus, Co^{2+} and Co^{3+} now hold effective negative charges, $Co_{Co}^{3/2\prime}$ and $Co_{Co}^{1/2\prime}$ respectively, whereas Co^{4+} is effectively positive; $Co_{Co}^{1/2\bullet}$.[21]

To account for the different valence states of cobalt, the disproportionation reaction is introduced as:

$$2Co_{Co}^{1/2\prime} \leftrightharpoons Co_{Co}^{1/2\bullet} + Co_{Co}^{3/2\prime} \quad (1)$$

From structural studies, it is also known that there are three different oxygen sites; one O1-site in the Ba-layer, one O3-site in the Ln-layer and four O2-sites in the Co-layer.[7, 8, 22] Oxygen vacancies preferentially form on the O3-site, whereas there are indications of some oxygen vacancies in the Co-O layer.[12, 15, 23, 24] The oxidation of oxygen vacancies on O3 sites can then be expressed as:

$$\frac{1}{2}O_2(g) + v_{O3}^{\bullet\bullet} + 2Co_{Co}^{1/2\prime} \leftrightharpoons O_{O3}^{x} + 2Co_{Co}^{1/2\bullet} \quad (2)$$

To allow oxygen vacancy formation also on O2-sites, an oxygen disorder reaction is introduced:

$$O_{O2}^{x} + v_{O3}^{\bullet\bullet} \leftrightharpoons v_{O2}^{\bullet\bullet} + O_{O3}^{x} \quad (3)$$

This yields the following set of equilibrium coefficients and balances for the BGLC system:

Oxidation
$$K_{ox} = \frac{[O_{O3}^{x}][Co_{Co}^{1/2\bullet}]^2}{[v_{O3}^{\bullet\bullet}][Co_{Co}^{1/2\prime}]^2} p_{O_2}^{-1/2} \quad (4)$$

Cobalt disproportionation
$$K_{cd} = \frac{[Co_{Co}^{1/2\bullet}][Co_{Co}^{3/2\prime}]}{[Co_{Co}^{1/2\prime}]^2} \quad (5)$$

Oxygen disorder

$$K_{\mathrm{od}} = \frac{[\mathrm{v}_{\mathrm{O2}}^{\bullet\bullet}][\mathrm{O}_{\mathrm{O3}}^{\mathrm{x}}]}{[\mathrm{v}_{\mathrm{O3}}^{\bullet\bullet}][\mathrm{O}_{\mathrm{O2}}^{\mathrm{x}}]} \quad (6)$$

Non-stoichiometry

$$\delta = [\,\mathrm{v}_{\mathrm{O2}}^{\bullet\bullet}] + [\,\mathrm{v}_{\mathrm{O3}}^{\bullet\bullet}] \quad (7)$$

Electroneutrality

$$\frac{3}{2}\left[\mathrm{Co}_{\mathrm{Co}}^{3/2\prime}\right] + \frac{1}{2}\left[\mathrm{Co}_{\mathrm{Co}}^{1/2\prime}\right] = \frac{1}{2}\left[\mathrm{Co}_{\mathrm{Co}}^{1/2\bullet}\right] + [\mathrm{La}_{\mathrm{Ba}}^{\bullet}] + 2\delta \quad (8)$$

Site balances

$$[\mathrm{O}_{\mathrm{O2}}^{\mathrm{x}}] + [\mathrm{v}_{\mathrm{O2}}^{\bullet\bullet}] = 4 \quad (9)$$

$$[\mathrm{O}_{\mathrm{O3}}^{\mathrm{x}}] + [\mathrm{v}_{\mathrm{O3}}^{\bullet\bullet}] = 1 \quad (10)$$

$$\left[\mathrm{Co}_{\mathrm{Co}}^{1/2\bullet}\right] + \left[\mathrm{Co}_{\mathrm{Co}}^{1/2\prime}\right] + \left[\mathrm{Co}_{\mathrm{Co}}^{3/2\prime}\right] = 2 \quad (11)$$

It may be noted that the mass action equilibrium coefficient expressions can be – and are – written without dividing by standard concentrations to obtain activities, because these standard concentrations in all cases cancel. The above set of equations is solved by first calculating the cobalt species concentrations for a given δ as:

$$\left[\mathrm{Co}_{\mathrm{Co}}^{1/2\bullet}\right] = -\frac{8\delta K_{\mathrm{cd}} - [\mathrm{La}_{\mathrm{Ba}}^{\bullet}] - 2\delta - 12K_{\mathrm{cd}} + B + 4[\mathrm{La}_{\mathrm{Ba}}^{\bullet}]K_{\mathrm{cd}} + 1}{2(4K_{\mathrm{cd}} - 1)} \quad (12)$$

$$\left[\mathrm{Co}_{\mathrm{Co}}^{1/2\prime}\right] = \frac{8dK_{\mathrm{cd}} - [\mathrm{La}_{\mathrm{Ba}}^{\bullet}] - 2\delta - 12K_{\mathrm{cd}} + B + 4[\mathrm{La}_{\mathrm{Ba}}^{\bullet}]K_{\mathrm{cd}} + 1}{(4K_{\mathrm{cd}} - 1)} - 2\delta - [\mathrm{La}_{\mathrm{Ba}}^{\bullet}] + 3 \quad (13)$$

Where the discriminant *B* is:

$$B = \sqrt{12K_{\mathrm{cd}} - 2[\mathrm{La}_{\mathrm{Ba}}^{\bullet}] + 4\delta + 16\delta K_{\mathrm{cd}} + 4\delta[\mathrm{La}_{\mathrm{Ba}}^{\bullet}] - 4[\mathrm{La}_{\mathrm{Ba}}^{\bullet}]^2 K_{\mathrm{cd}} - 16\delta^2 K_{cd} + [\mathrm{La}_{\mathrm{Ba}}^{\bullet}]^2 + 4\delta^2 + 8[\mathrm{La}_{\mathrm{Ba}}^{\bullet}]K_{\mathrm{cd}} - 16[\mathrm{La}_{\mathrm{Ba}}^{\bullet}]\delta K_{\mathrm{cd}} + 1} \quad (14)$$

By combining the oxygen interaction equilibrium (Eq. 6) with oxygen site balances (Eqs. 9 and 10) and inserting the cobalt concentrations from the expressions above (Eqs. 12 and 13), we obtain an expression for pO_2 as a function of δ which can be fitted to oxygen non-stoichiometry data:

$$pO_2^{1/2} = \frac{1}{K_{ox}} \cdot \frac{(1-\delta+A)\left[Co_{Co}^{1/2\bullet}\right]^2}{(\delta-A)\left[Co_{Co}^{1/2\prime}\right]^2} \tag{15}$$

Here, the discriminant A is given as:

$$A = \frac{4K_{od}-\delta+\delta\cdot K_{od}+1-\sqrt{\delta^2K_{od}^2-8\delta K_{od}+16K_{od}-2\delta^2K_{od}+10\delta K_{od}+8K_{od}+\delta^2-2\delta+1}}{2(K_{od}-1)} \tag{16}$$

Equation 15 is used to model experimental isotherms of δ vs pO_2 by adjusting and fitting the equilibrium constants K_{ox}, K_{cd} and K_{od}.

3. Experimental

3.1 Powder and sample preparation

Powders of BGLC (x = 0, 0.1, 0.2, 0.3 and 0.5) were prepared using combustion synthesis. Stoichiometric amounts of precursors, $Ba(NO_3)_2$ (99%), $Gd(NO_3)_3$, $6H_2O$ (99%), $La(NO_3)_3$,$6H_2O$ (99%) and $Co(NO_3)_2$,$6H_2O$ (99%), were first dissolved in water. Then urea, used as fuel, was introduced to the solution. The nitrates to fuel molar ratio was calculated considering the complete combustion of the precursors. The as-prepared solution was heated in air in a furnace at 600°C where an exothermic reaction occurs along with the ignition of the compound. The powder finally obtained through this solution combustion method was then calcined at 1100°C for 3h to form the required crystalline phase. After calcination a wet milling procedure with ZrO_2 balls was used to decrease the particle size of the powders. All powders were confirmed single phase double perovskites by XRD analysis, with an average grain size between 0.7 and 0.9 μm for all the powders.

Before testing the oxygen stoichiometry of these materials, the powders were heat-treated at 1050°C in air for 5 hours to coarsen the powders and minimize surface effects. Pellets for conductivity measurements were made by cold-pressing the powders in a steel die, before sintering at 1200°C for 2 hours with a ramp rate of 300°C/h, resulting in dense black pellets (>97% relative density) with 15 mm diameter and thicknesses ranging from 1 to 2 mm.

3.2 Chemical and electrical characterization

The absolute value of δ was determined by complete reduction of the double perovskite in 5% H_2 (balance Ar). The absolute oxygen content is determined by monitoring the oxygen loss during decomposition when switching from air to 5% H_2 at 700°C.[15] The equilibrium oxygen content of BGLC was determined by thermogravimetric analysis in a Netzsch STA 449 F1 thermobalance for powder characterization and a CI Electronics MK2 microbalance for characterization of pellets. Powder and pellet samples (~2 g) pre-annealed at 1050°C were

exposed to varying pO_2 in the temperature range 400°C to 750°C while monitoring the mass change until equilibration (typically 20-300 minutes depending on temperature and pO_2). The oxygen partial pressure was varied from 1 atm to 0.0001 atm by mixing O_2 with N_2 or He gas using an in-house gas mixer described elsewhere,[25] with flow rates of 50 $mLmin^{-1}$.

For direct observation of the oxidation thermodynamics of BGLC, simultaneous thermogravimetry and differential scanning calorimetry (NETZCH STA 449 C Jupiter) was employed, connected to a gas mixer similar to that used for the pure TG measurements. Heat flow and mass change is measured upon a change in the oxygen partial pressure, associated with the reduction/oxidation. Isothermal switches from 0.001 atm O_2 to 1 atm O_2 were conducted in the temperature range 500°C to 750°C. Details on the procedure and instrument calibration can be found in ref 26.[26]

Electrical conductivity in the van der Pauw geometry and Seebeck coefficients of pellet samples were determined using a modified ProboStat (NorECs, Norway) setup, described elsewhere in detail.[27] For the measurement of Hall-effect at different temperatures, a Lakeshore HMS7704 with a magnetic field of 1 T and an excitation current of 100 mA was used. Direct experimental access to the carrier concentration and mobility is - in principle - possible via measurements of the Hall effect. However, no significant Hall voltage signal was detected for BGLC upon cycling of the magnetic field at both room temperature and 500°C.

4. Results and discussion

4.1 Oxygen non-stoichiometry

Calculated oxygen content and average cobalt valence states are summarized in Table 1. As expected, the oxygen content increases with increasing concentration of La donors on Ba-site. Consequently, but interestingly, the average cobalt valence state also increases with increasing La content, contrary to typical donor doping behavior.

Table 1: Oxygen stoichiometry and cobalt valence state at 700°C in dry air as determined by thermogravimetric decomposition

x_{La}	6-δ	δ	Average Co valence
0	5.43	0.57	2.93
0.2	5.55	0.45	2.95
0.3	5.62	0.38	2.97
0.5	5.79	0.21	3.05

The oxygen contents listed in Table 1 are used as a fixed reference point for further isobar and isotherm thermogravimetric measurements of oxygen non-stoichiometry. Figure 2 presents isobar temperature dependencies of the equilibrium oxygen content for all compositions recorded in 0.15 atm O_2 balanced with N_2 (bottle dry). The compositions with higher La content display higher total oxygen content and less oxygen loss upon heating, illustrating a lower tendency for oxygen vacancy formation with increasing donor doping. Similar trends can be seen from the isotherm pO_2-dependencies exemplified in Figure 3 for $x = 0$ and $x = 0.5$, where a steeper pO_2-dependency is observed for $x = 0$.

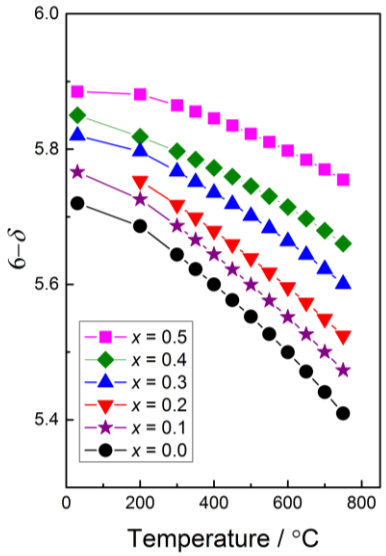

Figure 2: Equilibrium oxygen stoichiometry of BGLC (x = 0-0.5) in dry 0.15 atm O_2 determined by thermogravimetry (room temperature data not in equilibrium). The lines are guide-to-the-eye only.

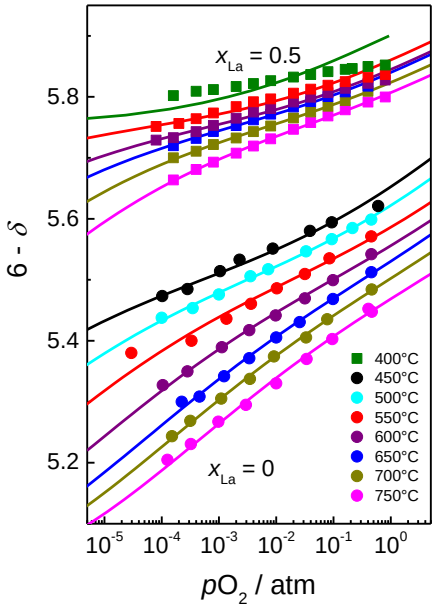

Figure 3: Isothermal oxygen stoichiometry of BGLC (x = 0 and 0.5) as a function of pO_2. The lines are the best fits obtained using Eq. 15.

The lines in Figure 3 represent the best fits using Equation 15. It is clear that the model enables accurate representation of the measured oxygen content in both un-doped and heavily doped BGLC. Similarly good fits were obtained also for $x = 0.2$ and 0.3 in the same temperature regime. Thus, we may conclude that the derived defect chemical model is generally applicable to $Ba_{1-x}Ln_xCo_2O_{6-\delta}$ double perovskites with large variations in cation stoichiometry.

We do, however, note a discrepancy between the predicted and measured oxygen content at low temperatures and high pO_2 where the measured oxygen content seems to level off towards 5.6 and 5.85 for $x = 0$ and $x = 0.5$, respectively, which is especially clear at 400°C for $x = 0.5$. This represents an average cobalt valence state of $Co^{3.1+}$ in both cases, indicating that there is an upper threshold for the concentration of electron holes incorporated into the material.

This deviation is similar to what is observed for $La_2NiO_{4+\delta}$,[28] where a double-logarithmic pO_2-dependency below the ideal 1/6 is observed at high oxygen activities. The anomalous behavior was attributed to a positive deviation from an ideal dilute system with an activity coefficient of holes greater than unity ($\gamma_p > 1$) when the concentration of electron holes exceeded ~0.03 per unit cell. In the case of BGLC, a positive deviation is observed for a cobalt valence state of $\sim Co^{3.1+}$, corresponding to a concentration of electron holes of ~0.2 per unit cell. Thus, the model is not completely valid for temperatures below 450°C unless the thermodynamic factor of holes is incorporated.

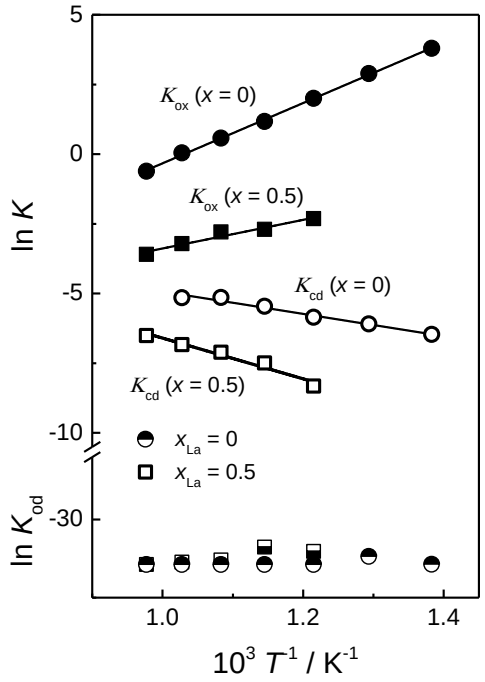

Figure 4: van 't Hoff plot displaying the natural logarithm of K_{ox}* (filled symbols), *K_{cd}* (open symbols) *and K_{od}* (half-filled symbols) *as a function of inverse temperature for compositions x = 0 (circles) and x = 0.5 (squares). The lines are linear fits used to extract ΔH^0 and ΔS^0 for each reaction.

The equilibrium constants obtained at each temperature are further plotted in a van 't Hoff plot to extract thermodynamic parameters, shown in Figure 4 for x = 0 and 0.5. Both the equilibrium constants for the oxidation reaction (K_{ox}) and the cobalt disproportionation reaction (K_{cd}) follow Arrhenius type behavior, whereas K_{od} for the oxygen disorder reaction is relatively constant with very small values at all temperatures. The latter indicates that oxygen vacancies are primarily located on O3-sites in the lanthanide layer, making the model insensitive to the contribution from O2 vacancies in the Co layer. Thus, standard enthalpies and entropies are only calculated for reactions 4 and 5, and presented in Table 2. The standard oxidation enthalpies for reaction 4 are between -45 and -60 kJ mol^{-1} for all compositions. The standard oxidation entropies range from -75 J mol^{-1} K^{-1} to -110 J mol^{-1} K^{-1}, comparable to the entropy change associated with the consumption of half a mole of gas. The enthalpies of cobalt dissociation range from 20 kJ mol^{-1} to 45 kJ mol^{-1}, close to values for cobalt double perovskites in the literature.[13, 14, 16-18] For cobalt disproportionation (Eq. 5), the entropy change is expectedly small (-10 to -30 J mol^{-1} K^{-1}), as no gas molecules are formed or consumed in the reaction.

Table 2: Thermodynamic parameters for the oxidation reaction (Eq.4) and the cobalt disproportionation reaction (Eq.5) obtained by linear fit of equilibrium constants shown in Figure 4.

	Oxidation Reaction		**Cobalt disproportionation**	
x_{La}	ΔH^0_{ox} (kJ mol^{-1})	ΔS^0_{ox} (J mol^{-1} K^{-1})	ΔH^0_{cd} (kJ mol^{-1})	ΔS^0_{cd} (J mol^{-1} K^{-1})
0	-60 $\pm$ 10	-110 $\pm$ 12	30 $\pm$ 9	-15 $\pm$ 10
0.2	-55 $\pm$ 7	-100 $\pm$ 8	25 $\pm$ 6	-20 $\pm$ 8
0.3	-55 $\pm$ 9	-95 $\pm$ 9	20 $\pm$ 13	-30 $\pm$ 13
0.5	-45 $\pm$ 15	-75 $\pm$ 20	45 $\pm$ 11	-10 $\pm$ 11

The defect chemical fitting presented in Figure 3 indicated that oxygen vacancies primarily form on O3 sites, and that formation of oxygen vacancies in the Co- or Ba-layers do not contribute significantly to the equilibrium oxygen content. This is in contrast to neutron diffraction studies of different double perovskites which found non-zero concentrations of oxygen vacancies in the Co-layer.[29, 30] It is, however, challenging to conclude on the presence of O2-vacancies based on defect chemical modelling of the present data set. To exemplify, Figure 5 presents the best fits of the thermogravimetric data using a fixed enthalpy of ΔH^0_{od} = -20 kJ mol^{-1} and zero entropy change (ΔS^0_{od} = 0) for the oxygen disorder reaction, resulting in a low, but non-zero concentration of oxygen vacancies in the Co-layer. The model remains in reasonable agreement with the data, albeit with larger discrepancies at low oxygen content. The obtained thermodynamic parameters for K_{ox} change slightly with fixed oxygen disorder parameters, whereas the cobalt disproportionation parameters remain essentially unchanged, as the latter is primarily influenced by the overall oxygen stoichiometry rather than the local oxygen ordering. Accordingly, we cannot definitively exclude the presence of O2-vacancies based on our work, but suffice to say that our model indicates that the concentration remains low compared to that of O3-vacancies.

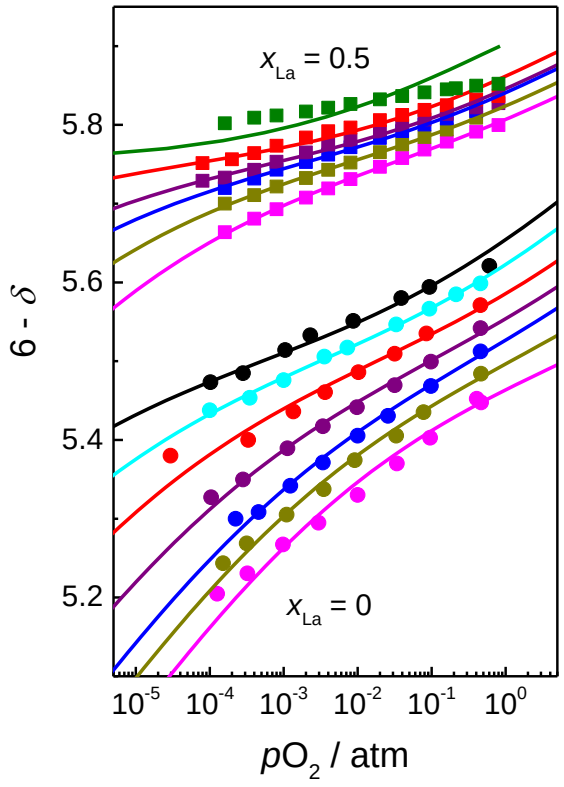

Figure 5: Isothermal oxygen stoichiometry for x = 0 and x = 0.5 fitted using a fixed enthalpy (ΔH^0 = 20 kJ mol^{-1}) and entropy (ΔS^0 = 0) for the oxygen disorder reaction.

The defect chemical modelling presented above aims to delineate macroscopic measurements of oxygen interaction into specific defect chemical reactions with individual thermodynamic parameters. Combined thermogravimetry and differential scanning calorimetry (TG-DSC) is a complementary technique which directly measures the macroscopic enthalpy of oxidation, allowing the independent verification of parameters obtained by defect chemical modeling.[26] Oxidation enthalpies obtained from a switch from N_2 to O_2 is presented in

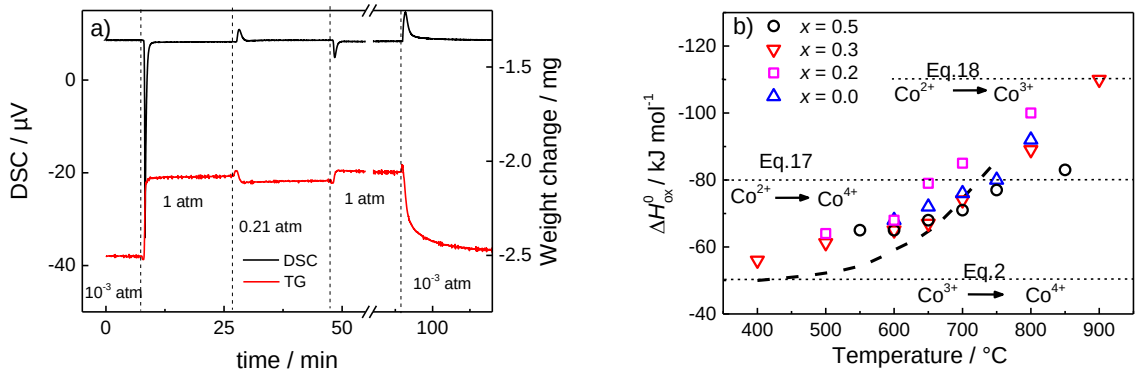

as a function of temperature for all compositions.

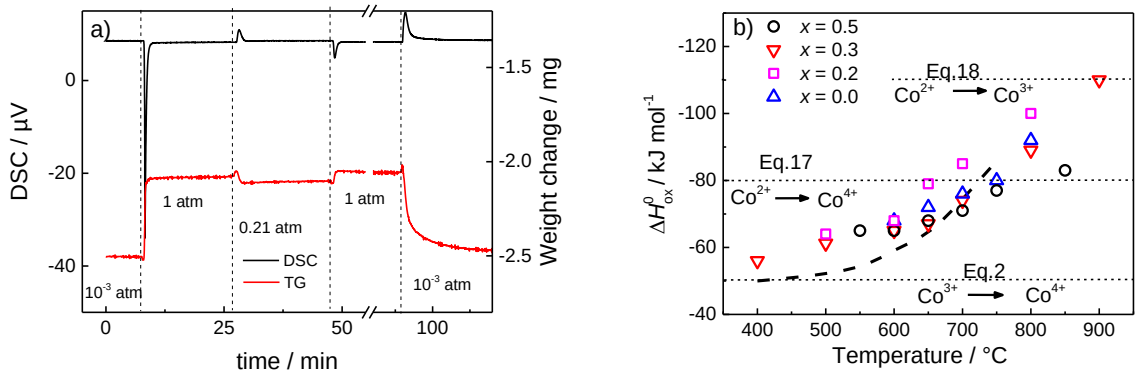

Figure 6: a) Representative TG-DSC data showing weight change (red) and DSC signal (black) upon changing oxygen partial pressure. b) Exothermic oxidation enthalpies of BGLC (x = 0-0.5) measured by TG-DSC as a function of temperature. The dotted line represent predicted net oxidation enthalpies from the defect chemical model for x = 0.5.

The measured enthalpies become slightly more exothermic with *x* at each temperature with increasing difference towards the higher temperatures. The oxidation enthalpies are generally more exothermic than the enthalpy of reaction 2 obtained from defect chemical modelling. These observations can be rationalized considering that the enthalpy measured by TG-DSC does not necessarily correspond to a single defect chemical reaction (e.g. Eq. 2), but is rather a measure of the total energy difference between the "reduced" and "oxidized" state. In the defect chemical modelling, we only considered one potential oxidation reaction, but due to the cobalt disproportionation reaction there are two other reactions that may contribute to the total oxidation:

$$\frac{1}{2}O_2(g) + v_{O3}^{\bullet\bullet} + Co_{Co}^{3/2\prime} \leftrightharpoons O_{O3}^{x} + Co_{Co}^{1/2\bullet} \quad (17)$$

$$\frac{1}{2}O_2(g) + v_{O3}^{\bullet\bullet} + 2Co_{Co}^{3/2\prime} \leftrightharpoons O_{O3}^{x} + 2Co_{Co}^{1/2\prime} \quad (18)$$

Equations 17 and 18 are simple linear combinations of the oxidation reaction (Eq. 2) and cobalt disproportionation (Eq. 1), and their thermodynamic parameters can thus be calculated from proper summation of the values in Table 2. Generally, the oxidation enthalpies are in the range -70-90 kJ mol^{-1} for Eq. 17 and -100-120 kJ mol^{-1} for Eq. 18. The total oxidation enthalpy will therefore depend on which oxidation reaction dominates at a given temperature, estimated from the net change in concentration of the different cobalt species upon going from N_2 to O_2. Figure 7a presents representative examples of cobalt species concentrations as a function of pO_2 at 500°C and 700°C for x = 0.2. At low temperature where the oxygen content is higher, oxidation of Co^{3+} to Co^{4+} is most prevalent, whereas oxidation of divalent cobalt contributes significantly to the overall oxidation reaction at higher temperatures. From this, we may calculate the expected net oxidation enthalpy from our defect chemical model, depicted with the dotted line in

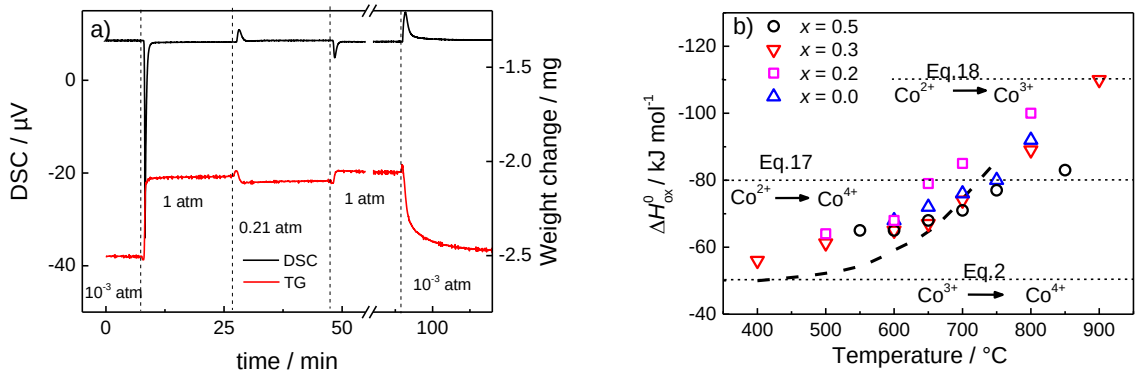

for x = 0.5, in good agreement with our TG-DSC data.

Oxygen stoichiometry-dependent oxidation enthalpies have been observed and discussed previously, for instance in the "itinerant electron model" by Lankhorst and Bouwmeester.[31, 32] Therein, the change in enthalpy is associated with an altered density of states at the Fermi level assuming a rigid band model, which correlates well with a changing concentration of reactants for the oxidation reactions described above.

4.2 Electrical conductivity

Figure 7b presents the electrical conductivities in air of all compositions measured in equilibrium by the van der Pauw 4-point method. All compositions display conductivities above 500 S cm^{-1}, typical for these cobalt-based double perovskites, but no apparent trend is observed as a function of lanthanum content, *x*. All compositions display a maximum in conductivity in the temperature range 300 to 500°C, followed by a steep decrease towards the higher temperatures. In the low temperature region (< 300°C), the temperature dependency is significantly steeper for $x = 0.5$ than for the unsubstituted sample which is almost temperature independent in this temperature range. Common for all compositions is a positive, but very shallow pO_2-dependency as exemplified in Figure 7c at 600°C.

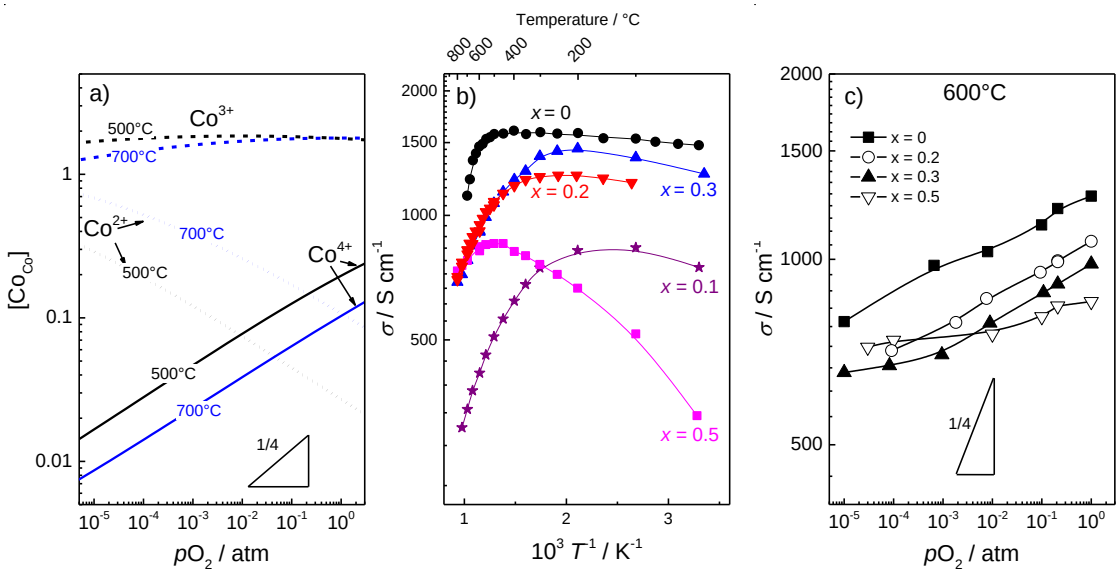

Figure 7: Calculated cobalt concentrations vs pO_2 (a) and measured electrical conductivities as a function of inverse temperature (b) and pO_2(c). Lines in b) and c) are guide-to-the-eye only.

We may broadly rationalize these observations as follows: The initial increase in conductivity as the temperature is increased from room temperature can be ascribed to a combination of increased mobility and increased charge carrier concentration due to intrinsic ionization (Eq. 1). Oxygen loss with increasing temperature is minimal in this temperature regime – as observed from TG measurements – and thus minimal annihilation of electron holes is expected. At higher temperature there is a significant loss of oxygen, leading to a depletion of electron holes upon further heating, which eventually compensates and overtakes the contribution from increasing ionization and mobility. However, the conductivity cannot be directly related to the concentration of holes present in the form of $Co_{Co}^{1/2\bullet}$ (Co^{4+}), as is easily recognized by the sizable difference in slopes of the conductivity and Co^{4+} concentration as a function of pO_2 (see Figure 7a).

From Figure 7b it is evident that the conductivity does not scale directly with the concentration of lanthanum donors (x) at any given temperature. This indicates an alteration of the energy states within heavily doped BGLC, which influences both the mobility and concentration of electronic charge carriers. To elucidate the origin of these variations, electrical conductivity is plotted vs the average cobalt valence state for all compositions in the temperature range 500 to

800°C in Figure 8. There is a clear linear correlation among all samples, underpinning that the average cobalt valence state is the prime determinant of the total conductivity. It is also evident that the conductivity scales inversely with the concentration of lanthanum donors for a given cobalt valence state, which suggests increased ionization energy (ΔH_{cd}) and/or decreased mobility for highly substituted BGLC.

We also note that the conductivity remains very high even with a cobalt oxidation state below 3, where the concentration of electrons far exceeds that of holes, suggesting that electronic conduction has contributions from both electrons and holes.

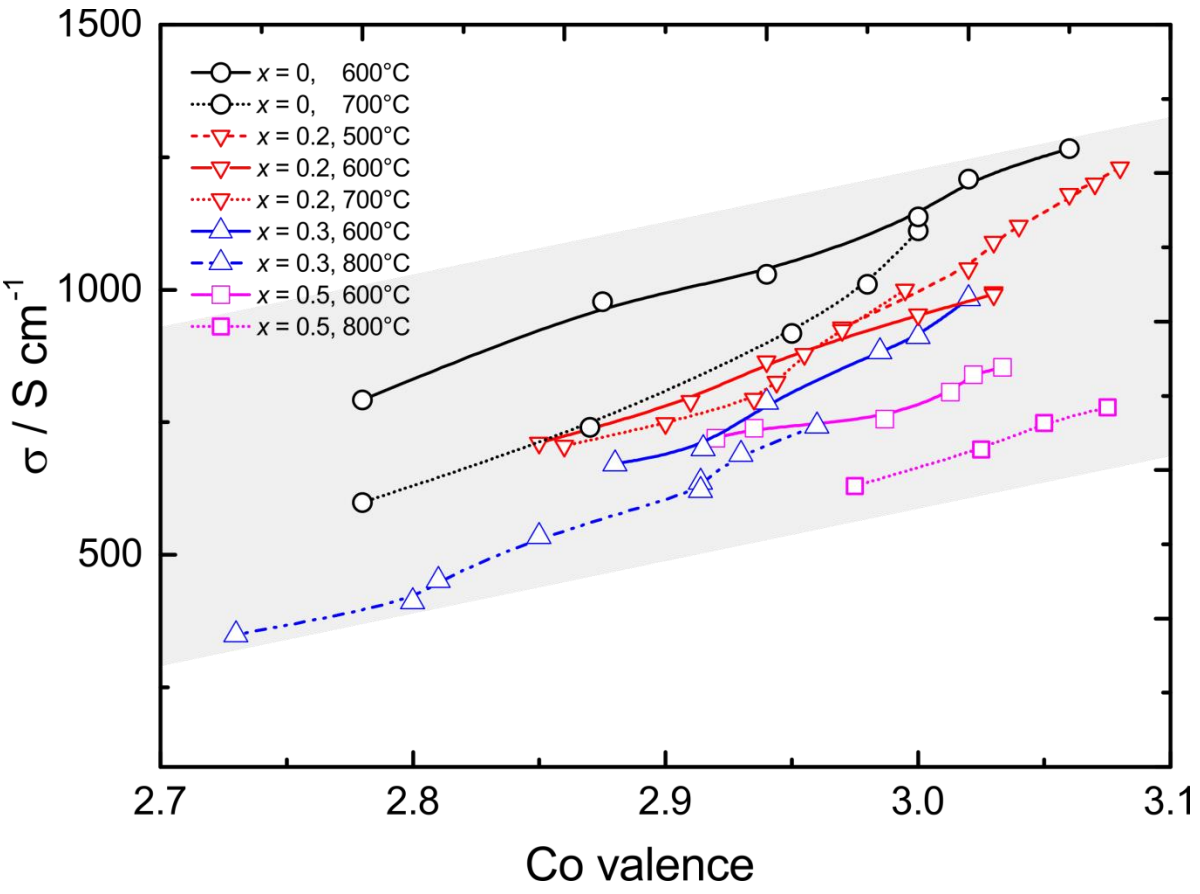

Figure 8: Electrical conductivity of different BGLC compositions as a function of average cobalt valence state calculated from oxygen stoichiometry determined by TG.

To further investigate the electronic transport mechanism, Seebeck and Hall measurements were conducted on several samples. Figure 9 presents the Seebeck coefficient vs. ln σ for x = 0 in a

typical Jonker plot,[33] where positive Seebeck coefficients reflect a predominantly p-type conduction mechanism. The absolute Seebeck coefficients are very small – comparable to that of good metals such as gold, silver and copper. For a non-degenerate p-type semiconductor, the slope of the Jonker plot should be $-k/e$= -86.15 µV/K, whereas the slope in our case is much smaller and close to -10 µV/K. A low slope and small absolute Seebeck coefficients combined with high electrical conductivities typically reflects large degree of degeneracy. This is further supported by Hall coefficients being below our detection limit, previously attributed to competing contributions from itinerant and localized charge carriers with large concentrations.[11]

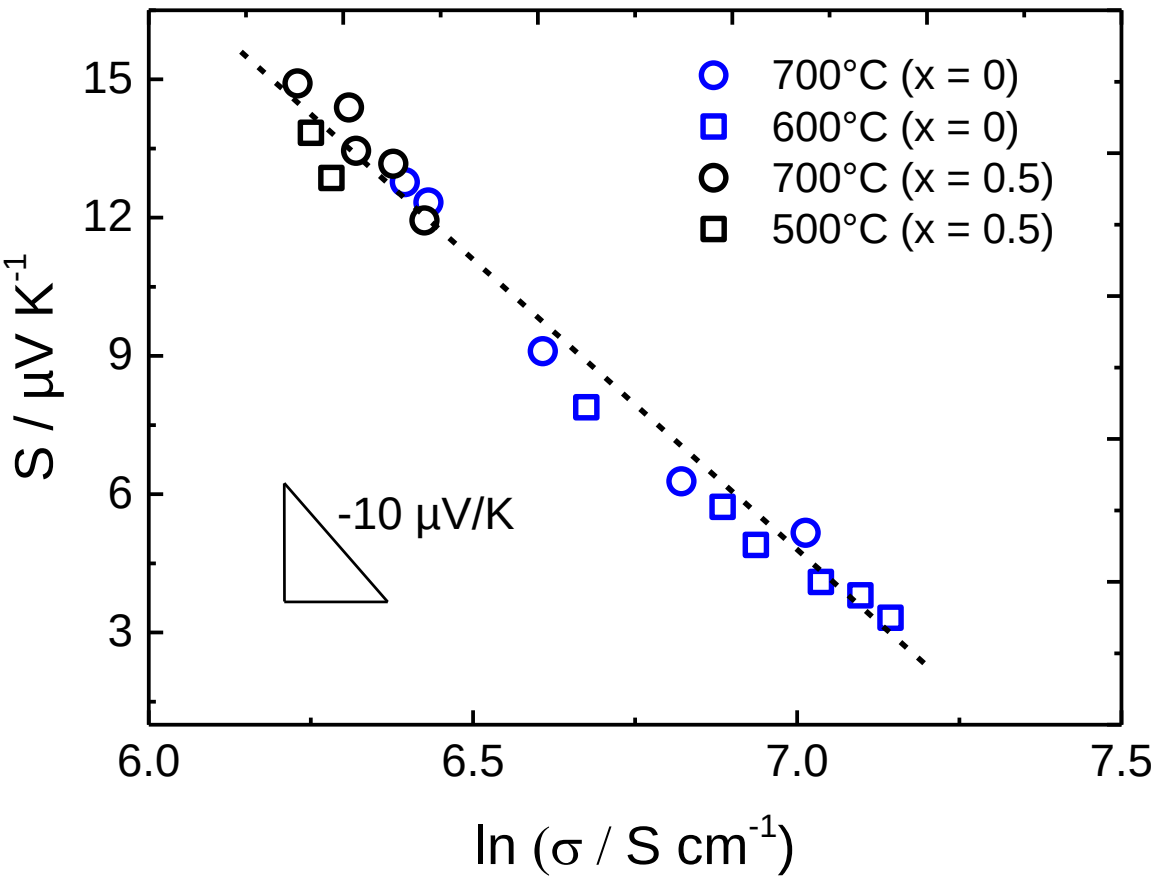

Figure 9: Jonker plot of Seebeck coefficient vs ln σ for x = 0 (blue) and x = 0.5 (black) at 500°C, 600°C and 700°C.

4.3 Correlating electrical conductivity and defect chemistry

From the present data set, it is clear that electronic transport in these double perovskites is not confined to simple p-type conduction in the form of oxidized Co^{4+} species. For some perovskite systems, it has been suggested that the increased conductivity with pO_2 could be attributed to an

increased mobility due to enhanced hybridization between Co3*d* and O2*p* orbitals with higher oxygen content.[34] In this case, we would expect a constant Seebeck coefficient with pO_2 as the thermopower is independent of electron mobility, whereas the Seebeck coefficient of BGLC decreases with pO_2, commonly attributed to increased carrier concentration.

Thus, our results rather indicate a two-band conduction mechanism comprising a highly mobile p-type charge carrier in parallel with a less mobile n-type charge carrier, as suggested by Taskin *et al*. based on combined Seebeck and Hall measurements at low temperatures.[11] The n-type charge carrier is traditionally attributed to localized electrons in the form of Co^{2+},[6, 11] such that the conductivity can be expressed as:

$$\sigma_{el} = ze\left(\mu_p[Co^{4+}] + \mu_e[Co^{2+}]\right) \quad (19)$$

In Figure 10, the electrical conductivity of BGLC (x = 0) at 600°C is plotted vs pO_2, with the dotted line representing the best fit to Eq. 19 by adjusting the mobility ratio. It is evident that the data is not concurrent with the model, as the model clearly predicts a minimum in conductivity close to the pO_2 where the average cobalt valence state is Co^{3+}, whereas we have seen that the conductivity is almost linear across this region.

Going back to our defect chemical model, a Co^{3+} was treated as effectively negative ($Co_{Co}^{1/2\prime}$), and may thus be considered as an electronic (n-type) charge in itself. In that case, the electrical conductivity can be expressed as:

$$\sigma_{el} = ze\left(\mu_p[Co^{4+}] + \mu_e[Co^{3+}]\right) \quad (20)$$

The solid line in Figure 10 represents the best fit obtained using Eq. 20 for the electrical conductivity, showing an excellent representation of the data. Similarly good fits are obtained for all compositions throughout the temperature range 500°C to 700°C. On this basis, it seems that the electrical conductivity of BGLC is best represented by a two-band conduction mechanism where highly mobile p-type charge carriers in the form of Co^{4+} reside in a broad band and less mobile n-type charge carriers in the form of Co^{3+} are transported in a narrower band.

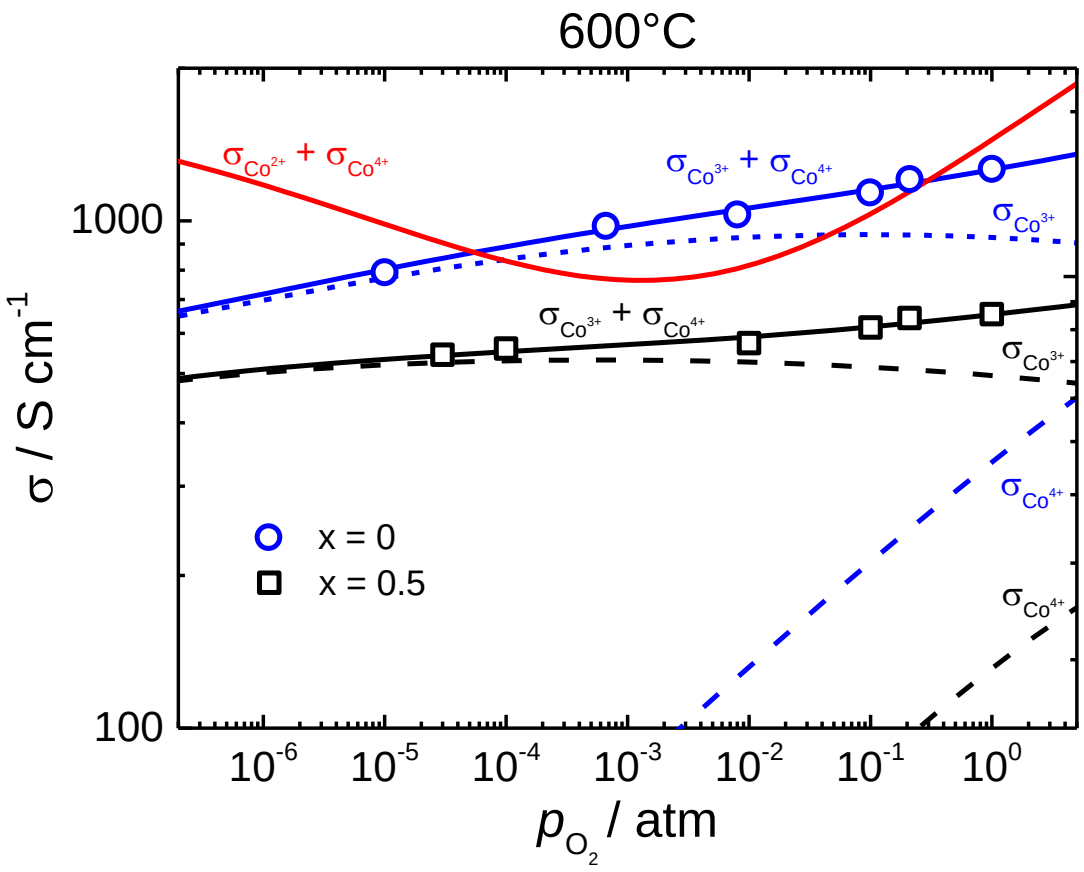

Figure 10: Electrical conductivity of BGLC, x = 0 (blue) and x = 0.5 (black) at 600°C vs pO_2. The solid lines are best fits to Eqs.19 (red) and 20 (black and blue).

The two-band conduction can be considered a result of the complex band structure of these double perovskites that arises from the overlap between Co*3d* orbitals and the O*2p* orbitals. The six d-electrons of Co^{3+} can take low-spin (LS), intermediate-spin (IS) or high-spin (HS) configurations in octahedral coordination. Based on theory developed by Goodenough,[19] it has been shown that both IS ($t_{2g}^5e_g^1$) and HS ($t_{2g}^4e_g^2$) Co^{3+} configurations are stable at elevated temperatures in $LnCoO_3$ and $Ln_{0.5}Sr_{0.5}CoO_3$,[20, 35, 36] resulting in partially occupied e_g states which form a narrow and partially occupied σ*-band through hybridization with oxygen orbitals.[6, 11] For the $BaLnCo_2O_{6-\delta}$ double perovskites, the σ*-band overlaps with the top of the valence band formed by hybridized O 2*p* states. As suggested by several authors, electron holes are formed within the highly delocalized valence band allowing fast p-type conduction.[20, 37] The σ*-band remains partially occupied with approximately one electron per two e_g states, enabling electronic

transport in a more narrow band constituted by IS Co^{3+} states. A schematic representation of such a band structure is presented in Figure 11.

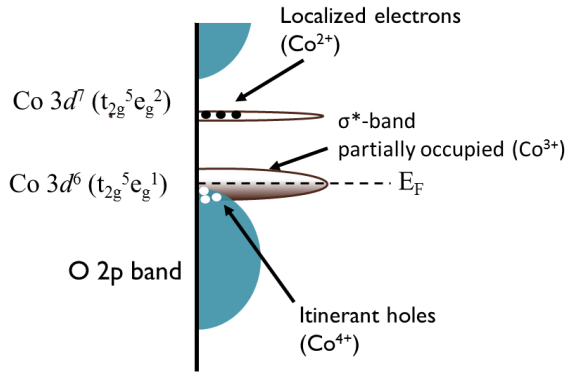

Figure 11: Schematic representation of a possible high temperature band structure of BGLC, illustrating a partially filled 3d band state located close to the top of the valence band.

5. Conclusions

Rare-earth double perovskites comprise a class of functional oxides with many interesting electrochemical and electrical properties due to the complex electronic structure arising from spin transitions of octahedrally coordinated cobalt ions. Here, we have studied the high temperature chemical and electrical properties of partially A-site substituted BGLC through thermogravimetry and electrical characterization. A comprehensive defect chemical model which is generally applicable over a large range of dopant concentrations is developed, and shows excellent correlation with measured oxygen content and oxidation thermodynamics from TG-DSC measurements. The defect chemistry of BGLC is further utilized to rationalize the high temperature electrical conductivity which exhibits traits of both localized small polarons and more metallic conduction. Based on combined Seebeck and conductivity measurements as a function of pO_2 for a range of compositions and temperatures, the conductivity is found to comprise two parallel electronic charge carriers; highly mobile p-type charge carriers in the broad O *2p*-band and less mobile n-type charge carriers in a partially occupied σ*-band formed by degenerate spin states of the Co *3d* electrons.

6. Acknowledgements

The research leading to these results has received funding from the European Union's Seventh Framework Programme (FP7/2007-2013) for the Fuel Cells and Hydrogen Joint Technology Initiative under grant agreement n° 621244. Dr. Matthias Schrade also acknowledges funding RCN project “THELMA” (NFR 228854).

7. References

1. R. Strandbakke, V. A. Cherepanov, A. Y. Zuev, D. S. Tsvetkov, C. Argirusis, G. Sourkouni, S. Prünte and T. Norby, *Solid State Ionics*, 2015, **278**, 120-132.
2. H. Ding and X. Xue, *International Journal of Hydrogen Energy*, 2010, **35**, 4311-4315.
3. F. Dong, M. Ni, Y. Chen, D. Chen, M. O. Tade and Z. Shao, *Journal of Materials Chemistry A*, 2014, **2**, 20520-20529.
4. Y. Lin, R. Ran, Y. Zheng, Z. Shao, W. Jin, N. Xu and J. Ahn, *Journal of Power Sources*, 2008, **180**, 15-22.
5. G. Kim, S. Wang, A. Jacobson, L. Reimus, P. Brodersen and C. Mims, *Journal of Materials Chemistry*, 2007, **17**, 2500-2505.
6. A. A. Taskin and Y. Ando, *Physical Review Letters*, 2005, **95**, 176603.
7. J.-H. Kim and A. Manthiram, *Journal of Materials Chemistry A*, 2015, **3**, 24195-24210.
8. T. Nakajima, M. Ichihara and Y. Ueda, *Journal of the Physical Society of Japan*, 2005, **74**, 1572-1577.
9. S. L. Pang, X. N. Jiang, X. N. Li, Q. Wang and Q. Y. Zhang, *Materials Chemistry and Physics*, 2012, **131**, 642-646.
10. C. Frontera, Garcı, amp, x, J. L. a-Muñoz, A. Llobet, L. Mañosa and M. A. G. Aranda, *Journal of Solid State Chemistry*, **171**, 349-352.
11. A. A. Taskin, A. N. Lavrov and Y. Ando, *Physical Review B*, 2005, **71**, 134414.
12. C. Bernuy-Lopez, K. Høydalsvik, M.-A. Einarsrud and T. Grande, *Materials*, 2016, **9**, 154.
13. A. N. Petrov, V. A. Cherepanov and A. Y. Zuev, *Journal of Solid State Electrochemistry*, 2006, **10**, 517-537.
14. A. Y. Suntsov, I. Leonidov, M. Patrakeev and V. Kozhevnikov, *Journal of Solid State Chemistry*, 2013, **206**, 99-103.
15. A. Y. Suntsov, B. Politov, I. Leonidov, M. Patrakeev and V. Kozhevnikov, *Solid State Ionics*, 2016, **295**, 90-95.
16. D. Tsvetkov, M. Ananjev, V. Eremin, A. Y. Zuev and E. K. Kurumchin, *Dalton Transactions*, 2014, **43**, 15937-15943.
17. D. Tsvetkov, V. Sereda and A. Y. Zuev, *Solid State Ionics*, 2010, **180**, 1620-1625.

18. D. Tsvetkov, V. Sereda and A. Y. Zuev, *Solid State Ionics*, 2011, **192**, 215-219.
19. J. B. Goodenough, *Materials Research Bulletin*, 1971, **6**, 967-976.
20. R. Potze, G. Sawatzky and M. Abbate, *Physical Review B*, 1995, **51**, 11501.
21. T. Norby, *Journal of the Korean Ceramic Society*, 2010, **47**, 19-25.
22. H. Shiiba, M. Nakayama, T. Kasuga, R. W. Grimes and J. A. Kilner, *Physical Chemistry Chemical Physics*, 2013, **15**, 10494-10499.
23. M. B. Choi, S. Y. Jeon, J. S. Lee, H. J. Hwang and S. J. Song, *Journal of Power Sources*, 2010, **195**, 1059-1064.
24. N. Ishizawa, T. Asaka, T. Kudo, K. Fukuda, A. Yasuhara, N. Abe and T.-h. Arima, *Chemistry of Materials*, 2014, **26**, 6503-6517.
25. T. Norby, *Solid State Ionics*, 1988, **28**, 1586-1591.
26. M. Schrade, S. Casolo, P. J. Graham, C. Ulrich, S. Li, O.-M. Løvvik, T. G. Finstad and T. Norby, *The Journal of Physical Chemistry C*, 2014, **118**, 18899-18907.
27. M. Schrade, H. Fjeld, T. Norby and T. G. Finstad, *Review of Scientific Instruments*, 2014, **85**, 103906.
28. H.-S. Kim and H.-I. Yoo, *Physical Chemistry Chemical Physics*, 2010, **12**, 4704-4713.
29. R. A. Cox-Galhotra, A. Huq, J. P. Hodges, C. Yu, X. Wang, W. Gong, A. J. Jacobson and S. McIntosh, *Solid State Ionics*, 2013, **249**, 34-40.
30. I. Seymour, A. Tarancon, A. Chroneos, D. Parfitt, J. Kilner and R. Grimes, *Solid State Ionics*, 2012, **216**, 41-43.
31. M. H. Lankhorst, H. Bouwmeester and H. Verweij, *Journal of solid state chemistry*, 1997, **133**, 555-567.
32. M. H. Lankhorst, H. J. Bouwmeester and H. Verweij, *Journal of the American Ceramic Society*, 1997, **80**, 2175-2198.
33. G. H. Jonker, *Philips Research Reports*, 1968, **23**, 131-&.
34. V. Sereda, D. Tsvetkov, I. Ivanov and A. Y. Zuev, *Journal of Materials Chemistry A*, 2015, **3**, 6028-6037.
35. C. Zobel, M. Kriener, D. Bruns, J. Baier, M. Grüninger, T. Lorenz, P. Reutler and A. Revcolevschi, *Physical Review B*, 2002, **66**, 020402.
36. M. A. Korotin, S. Y. Ezhov, I. V. Solovyev, V. I. Anisimov, D. I. Khomskii and G. A. Sawatzky, *Physical Review B*, 1996, **54**, 5309-5316.
37. A. Grimaud, K. J. May, C. E. Carlton, Y.-L. Lee, M. Risch, W. T. Hong, J. Zhou and Y. Shao-Horn, *Nature Communications*, 2013, **4**, 2439.